Dalton Transactions

ROYAL SOCIETY OF CHEMISTRY

PAPER

View Article Online
View Journal | View Issue

Cite this: *Dalton Trans.*, 2025, **54**, 5136

Heterogenous HER activity of Ni(II)N_2S_2 molecular catalysts†

Mohan Paudel, [a] Sanjit Karki, [a] Narayan Acharya, [a] Sashil Chapagain, [a] Johann V. Hemmer, [a] Dillon T. Hofsommer, [a] Gautam Gupta, *[b] Robert M. Buchanan *[a] and Craig A. Grapperhaus *[a]

Received 1st January 2025,
Accepted 21st February 2025

DOI: 10.1039/d5dt00005j

rsc.li/dalton

Green hydrogen, generated through the electrolysis of water using renewable energy sources, is recognized as a highly promising alternative to fossil fuels in the pursuit of net-zero carbon emissions. Electrocatalysts are crucial for reducing overpotentials and enhancing the efficiency of the hydrogen evolution reaction (HER) for the production of green hydrogen. Homogeneous HER serves as a primary method to assess the activity and mechanisms of novel non-precious molecular electrocatalysts in pursuit of replacing precious platinum standards. However, these catalysts can sometimes exhibit instability under reductive and acidic conditions during homogeneous HER. Thus, it is also essential to evaluate catalysts through heterogeneous HER for initial assessment and practical application. In this study, we examine a series of structurally related N_2S_2 chelated Ni(II) complexes, which are tailored to optimize the basicity of the catalyst for heterogeneous HER activity. These complexes are insoluble in 0.5 M H_2SO_4, and the films formed after catalyst deposition on glassy carbon electrodes (GCEs) exhibit catalytic currents during HER, demonstrating moderate to good overpotentials, Tafel slopes, and charge transfer resistance. Furthermore, we observe the anticipated structure–activity relationship that arises from tuning the catalyst structure. The complexes maintain stability over extended reductive cycling, as confirmed by various surface characterization techniques, including SEM, EDX, XPS, and XRD. This study highlights the potential of utilizing catalyst basicity to develop efficient and robust heterogeneous HER catalysts.

Introduction

Hydrogen is a viable alternative energy carrier to replace fossil fuels due to its high energy density and low emissions during combustion or use in fuel cells.[1,2] Green hydrogen, which is generated by water splitting using renewable energy sources, is particularly interesting as it represents an environmentally friendly method of H_2 production that excludes CO_2 emissions.[3] The most efficient electrocatalyst for the hydrogen evolution reaction (HER) is Pt/C, which operates at very low overpotentials.[4] However, the scarcity of Pt and its high costs limit its use in industrial-scale electrolyzers.[5] In addition, the electrocatalytic efficiency of Pt/C diminishes over time as a result of surface corrosion from prolonged exposure to strongly acidic or basic electrolytic conditions.[6] This has prompted the search for efficient, durable, low-cost alternatives.

Considerable effort has focused on the use of transition metal catalysts,[7] non-metal carbon-based catalysts,[8–10] metal alloys,[8,9] metal–organic frameworks,[9,11] and metals and mixed metal oxides,[12] phosphides[9,13] or nitrides[14,15] as HER electrocatalysts. Molecular catalysts containing inexpensive earth-abundant metals coordinated by one or more ligands are of particular interest as their physical and electronic structures can be tuned to modulate catalytic activity, which makes them excellent candidates for structure–activity studies.[16] Our group and others have studied redox active thiosemicarbazone-based molecular catalysts incorporating earth-abundant metals such as nickel, copper, and zinc as promising homogenous electrocatalysts demonstrating ligand-assisted metal-center,[17–19] metal-assisted ligand-centered,[20,21] and ligand-centered[22,23] HER mechanisms as a function of the metal and the ligand. A significant concern of homogeneous molecular HER catalysts is their potential instability in solution under acidic and/or reducing conditions, which can yield heterogenous, catalytically active degradation products.[24–26]

Recently, we reported the homogeneous HER activity of six structurally related Ni(II)N_2S_2 complexes with bis(thiosemicarbazonato) (BTSC) (**Ni-1**, **Ni-4**), thiosemicarbazonato-alkylthiocarbamato (TSTC) (**Ni-2**, **Ni-5**), and bis(alkylthiocarbamato) (BATC) (**Ni-3**, **Ni-6**) ligands (Fig. 1) in acetonitrile using acetic

[a]*Department of Chemistry, University of Louisville, 2320 S. Brook St, Louisville, KY 40292, USA. E-mail: robert.buchanan@louisville.edu, grapperhaus@louisville.edu*
[b]*Department of Chemical Engineering, University of Louisville, Louisville, Kentucky 40292, USA*

† Electronic supplementary information (ESI) available. See DOI: https://doi.org/10.1039/d5dt00005j

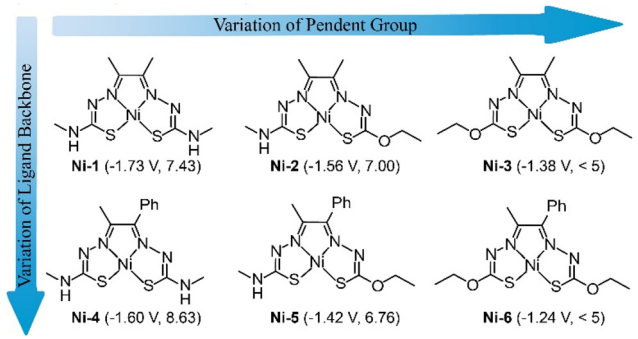

Fig. 1 Structures of complexes **Ni-1–Ni-6**. The values in the parenthesis are the experimental potentials for ligand-centered reduction in acetonitrile and calculated pK_a values for the hydrazine nitrogen respectively.

acid as proton donor.[27–29] The complexes in that study displayed a systematic decrease in reduction potentials, progressing from NiBTSC to NiTSTC to NiBATC. The computational study indicates over 91% of the spin density of mono reduced derivative [NiL$^-$] of all the complexes is localized on the ligand indicating the first reductions are ligand centered. This trend is accompanied by a reduction in ligand basicity as quantified by pK_a measurements using hydrogen triphenylphosphonium tetrafluoroborate as proton source (see Fig. 1). Computational exploration of the heteroatoms demonstrates protonation is most favored at the hydrazino nitrogen resulting in the formation of [NiLH]. Despite these structural and electronic differences, **Ni-1–Ni-6** exhibited nearly identical HER overpotentials that were similar to the Ni(II) salt Ni(OTf)$_2$. These results strongly suggested decomposition of the homogeneous catalysts upon exposure to a combination of reducing and acidic conditions.[30] In the current study, complexes **Ni-1–Ni-6** were immobilized on an electrode surface to evaluate how translation from homogeneous to heterogeneous conditions influenced HER activity and catalyst stability. The immobilized catalysts were evaluated before and after HER using a variety of spectroscopic, microscopic, and electrochemical methods.

Experimental

Materials and methods

All chemicals and solvents were used as purchased from commercial sources unless otherwise indicated. Solvents were dried using an MBraun Solvent Purification System. The syntheses and characterization of complexes **Ni-1–Ni-6** followed previously reported procedures.[30–33] All the compounds used in this study are air and water stable solids and reactions were conducted in open air under ambient conditions unless otherwise noted.

Ink preparation and electrode modification

Inks were prepared by dissolving a 4 mg sample of each complex (**Ni-1–Ni-6**) and controls (40% Pt/C and Ni(OTf)$_2$) in 1 mL of acetonitrile (VWR, ACS grade, dried using an MB-SPS from MBraun) using a vortex mixer (Vortex Genie 2, Scientific Industries). A 40 μL aliquot of a 10% aqueous Nafion solution was added. The dispersion was homogenized *via* ultrasonication (Cole-Parmer ultrasonic bath) for 30 minutes. Glassy carbon electrodes (GCE) (E4TQ ChangeDisk, Pine Research) were sonicated in ethanol and DI water for 15 minutes and then polished using an alumina slurry before each electrochemical study. They were further cleaned electrochemically by cycling from 1.2 V to −1.2 V *vs.* RHE in 0.5 M H_2SO_4 for 20 cycles. Finally, the electrodes were tested with ferricyanide solution to verify the absence of any contaminants before drop casting the catalyst ink. 14.5 μL of the catalyst ink was drop cast onto a cleaned GCE disc (drop cast density of 0.28 mg cm^{-2}) and rotated using a MSR Rotator (Pine Research) at 50 rpm until approximately half of solvent evaporated. The rotation speed was then increased to 300 rpm and maintained until the film dried.

Heterogeneous HER activity

The HER activity of the modified electrodes was evaluated using a three-electrode glass electrochemical cell (RDE/RRDE Cell Without Water Jacket, Pine Research) containing 0.5 M H_2SO_4 (VWR, ACS grade) prepared with twice-deionized Millipore water (18.2 Ω cm). A graphite rod (Pine Research) fitted in a protective fritted glass tube (Pine Research) was used as the counter electrode. Ag/AgCl (1 M KCl, CH Instruments) was used as the reference electrode. High-purity N_2 gas provided by Welders Supply, Louisville, KY, was used to sparge the solution during electrochemical studies. A Metrohm Autolab PGSTAT302N potentiostat/galvanostat, operating in potentiostatic mode, was used to obtain polarization and frequency response analysis (FRA) data. Reductive cycling was carried out to activate the catalyst and evaluate its stability between 0 and −0.8 V *versus* RHE at 100 mV s^{-1}. Linear sweep voltammetry (LSV) was carried out intermittently throughout the process after every 100 cycles, from 0 to −0.8 V *versus* RHE at 1 mV s^{-1}, to evaluate the catalyst activity at a relatively high resolution after multiple analyses at reductive potentials. Electrochemical impedance spectroscopy (EIS) was performed by FRA with data collected with an applied direct-current bias of −0.3 V *versus* RHE, starting at 100 kHz and finishing at 0.1 Hz, with 10 mV RMS amplitude. The working electrode was rotated at 1000 rpm throughout electrochemical characterization to facilitate diffusion of H_2 gas during HER from the catalyst surface. Measured potentials were calibrated *versus* RHE and corrected for *iR* by multiplying the measured current at each point by the real component of resistance measured at 100 kHz and then subtracting these values from the corresponding applied potentials.

The evolution of H_2 was confirmed using an H-cell fitted with a gas-tight "low-volume cell cap kit" (Pine Research) equipped with an Ag/AgCl reference, gas dispersion tube, gas outlet, and the working electrode coated with catalyst. The Pt mesh counter electrode was separated from the working electrode compartment by a Nafion 115 membrane, and each side

was filled with 0.5 M H_2SO_4. Chronopotentiometry at −10 mA cm^{-2} was performed for 120 minutes under a continuous stream of N_2 at a flow rate of 15 sccm and 1 mL of gas was sampled every 5 minutes by an in-line gas chromatographer (SRI Instrument, Multiple Gas Analyzer #1 + Sulfur). faradaic efficiencies were quantified by comparing the number of moles of charge used for H_2 production with the total number of moles of electrons supplied during the measurement.

Characterization methods

Catalyst inks prepared as described above were drop cast on the sample holder and dried to obtain the X-ray diffraction (XRD) pattern of the film before reductive cycling. The XRD pattern of the catalyst after cycling was obtained by scraping the catalyst from the GCE and loading it to the sample holder. All XRD data were collected at room temperature using Cu $K_{\alpha 1}$ radiation (λ = 1.54056 Å) on an X-ray diffractometer equipped with a Johansson monochromator. The 2θ scan range was 20–80°, and measurements were done with a step size of 0.0167°.

Scanning electron microscopy (SEM) images were obtained using an Apreo 2 C field emission scanning electron microscope (Thermo Fischer Scientific). Images of the catalyst materials before and after 1000 reductive CV cycles were obtained by removing the disk tip of the modified electrode. An Everhard-Thornley detector (ETD) in secondary electrode mode was used to analyze the catalyst surface. Samples were analyzed normal to the electrode beam, 2 mm from the cone. Accelerating high voltages and beam current were 2 kV and 6.3 pA, respectively. Elemental analysis and imaging were conducted using an Apreo 2 C field emission scanning electron microscope (Thermo Fischer Scientific) using a QUANTAX Energy-Dispersive X-ray (EDX) detector (Bruker). A voltage of 20 kV and a spot size of 10 were used for imaging, while a primary energy of 40 keV was used for EDX spectrometry. Images were collected 8.5 mm normal from the sample surface.

X-ray photoelectron spectroscopy (XPS) studies were performed using a VG Scientific Multilab 300 equipped with an AlK_α (1486.6 eV)/MgK_α (1253.6 eV) X-ray twin source, acceleration voltage of 10 kV, and emission current of 12 mA for the X-ray source. The electron energy analyzer operated in Fixed Analyzer Transmission (FAT) mode with a constant energy of 50 eV passed for survey and 20 eV for high-resolution scans.

Results and discussion

Synthesis and characterization

The series of structurally related Ni(II) N_2S_2 complexes, Fig. 1, was synthesized following previously reported procedures.[30–32] The purity of these complexes was confirmed by comparison with previously reported NMR, IR, and UV-visible spectroscopic data. Inks of **Ni-1**–**Ni-6** and controls (40% Pt/C and Ni $(OTf)_2$) were prepared in acetonitrile (1 mL) containing Nafion (40 μL of a 10% aqueous solution). The resulting suspensions were homogenized by ultrasonication followed by a drop cast on clean GCE discs to obtain the modified GCEs **1–6** and controls (40% Pt/C and Ni$(OTf)_2$) with a drop cast density of ~0.28 mg cm^{-2}. The surface structure and composition of the complexes were analyzed by SEM, energy-dispersive X-ray (EDX) spectroscopy, XPS, and XRD (*vide infra*).

Hydrogen evolution reaction

The HER activity of GCEs **1–6** and controls (40% Pt/C and Ni $(OTf)_2$) was analyzed using LSV, EIS measurements, and Tafel plot analysis. The modified electrodes were conditioned by cycling the potential between 0 V to −0.8 V *vs.* RHE at 100 mV s^{-1} for 1000 cycles. EIS and LSV data were collected after every 100 cycles. Overpotentials were measured at the current density of −10 mA cm^{-2}. Before reductive cycling, **1–6** showed comparable overpotentials (Fig. S1a†). The effect of reductive cycling electrodes **1–6** is shown in Fig. S2–S7† and summarized in Fig. S8† with peak activity highlighted in Fig. 2a and Table S1.† Interestingly, reductive cycling of **1** and **2**, which contain molecules with at least one NH-methyl pendent group, decreased the overpotential significantly from 0.76 V to 0.39 V and 0.72 V to 0.40 V, respectively. In a prior study, Gupta *et al.* observed a similar improvement in overpotential for **Ni-1** drop cast on GCE after reductive cycling. It was proposed that reductive cycling improves catalytic activity through dynamic surface reorganization, which involves exposure of catalytically active sites during hydrogen production and increases the electrochemically active surface area as measured by capacitance measurement in non-faradaic region and from Randles–Sevcik equation using ferrocyanide/ferricyanide as redox couple.[27,29] To demonstrate that reductive cycling is essential for catalyst activation, a constant potential of −0.40 V was applied for 10 hours to **2** before and after cycling. Prior to cycling, no current was observed. However, after 400 reductive cycles, a constant current density of 8.5 mA cm^{-2} was observed (Fig. S21†).

Modified electrodes **4** and **5** contain molecules with at least one NH-methyl pendent as in **1** and **2**, but with the substitution of a methyl group in the ligand backbone with a phenyl group. As shown in Fig. 2a, **4** and **5** show similar improvements in overpotential converging to 0.52 V from initial 0.70 V and 0.76 V, respectively, after peak reductive cycling. In comparison to **1** and **2**, the overpotentials for **4** and **5** have increased by ~0.12 V. Interestingly, **3** and **6**, which contain BATC complexes with electron-withdrawing O-ethyl pendent groups instead of electron-donating NH-methyl groups, show no significant improvement in overpotential even after 1000 CV cycles. In addition, **3** and **6** display similar overpotentials (0.670 V at peak reductive cycle) despite different ligand backbone substituents on the immobilized complexes.

The observed changes in overpotential for **1–6** upon reductive cycling are consistent with modification of the ligand structure of the immobilized complexes (Fig. 2b). Notably, electrodes with complexes that are easiest to reduce, **3** and **6**, have the highest overpotential. Rather, the overpotential for the optimized electrodes **1–6** depends on the basicity and

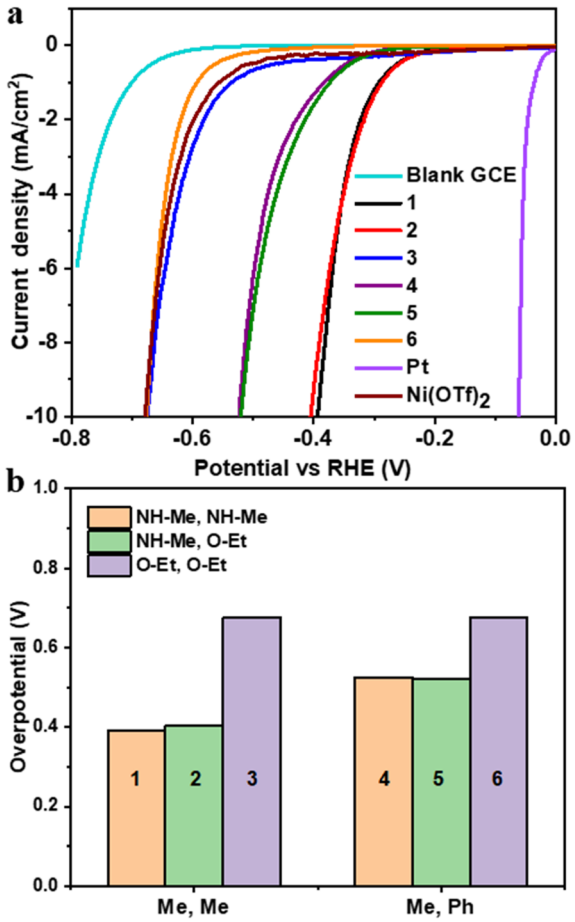

Fig. 2 (a) LSV of electrodes **1–6** compared to GCE, Pt, and $Ni(OTf)_2$ standards after peak reductive cycling (400 cy, 400 cy, 900 cy, 100 cy, 700 cy and 100 cy for **1–6**, respectively) in 0.5 M aq. H_2SO_4 and (b) graphical representation of the overpotential (at current density of -10 mA cm^{-2}) trend for **1–6** with changes in the pendent group (NH-Me or O-Et) and ligand backbone (Me, Me or Me, Ph).

steric accessibility of the hydrazine nitrogen in the catalyst. Complexes **Ni-3** and **Ni-6** have non-basic O-Et pendent groups,[30] and the largest overpotentials. The four other catalysts all have at least one pendent –NHMe group that is basic with pK_a values between 6.88 and 7.61.[30] The lowest overpotential is observed with **1** and **2** when the pendent –NHMe group is part of a ligand with only Me groups in the ligand backbone. Overall, the results indicate that peak overpotential is determined by the ease of protonation of the immobilized complex.

Hydrogen production was confirmed through gas chromatography and faradaic efficiencies for **1–6** were calculated using the methodology described in the Experimental section. Overpotentials for each electrode remained relatively constant over 75 minutes and faradaic efficiency values were found to be in the range of 86–92%, which is comparable to values measured for platinum (94%) (Fig. S36–S42†). The kinetics associated with HER for **1–6** were evaluated based on their Tafel slopes. Theoretically, a Tafel slope of 30, 40, or 120 mV dec^{-1} corresponds to a rate-determining Tafel step ($H^* + H^* \rightarrow H_2$), Volmer step ($H^+ + e^- \rightarrow H^*$), or Heyrovsky step ($H^* + H^+ + e^- \rightarrow H_2$), respectively. Deviation from these theoretical values can occur with the surface coverage of the catalyst and the applied potential.[34] The Tafel slopes for **1–6** after peak reductive cycling lie between 80 and 130 mV dec^{-1}, Fig. 3a and Table 1. This is most consistent with a Heyrovsky rate-determining step. Data showing the effect of reductive cycling on the Tafel slope are provided in Fig. S9–S14 and Table S2.†

Electrode characterization

Electrochemical impedance spectroscopy (EIS) was conducted using frequency response analysis (FRA) measurements, as detailed in the Experimental section. Charge transfer resistance (R_{ct}) corresponding to the diameter of the semicircle in the Nyquist plot was obtained by fitting the plot using Z-view. Prior to reductive cycling, electrodes **1–6** show a very high charge transfer resistance (Fig. S15–S20†). After peak reductive cycling, a marked reduction in the charge transfer resistance is observed. Similar results were reported by Gupta *et al.*[27] and is attributed to the reorganization of the catalyst surface, which improves contact between the catalyst and electrode surface and facilitates better charge transfer in the film. The Nyquist

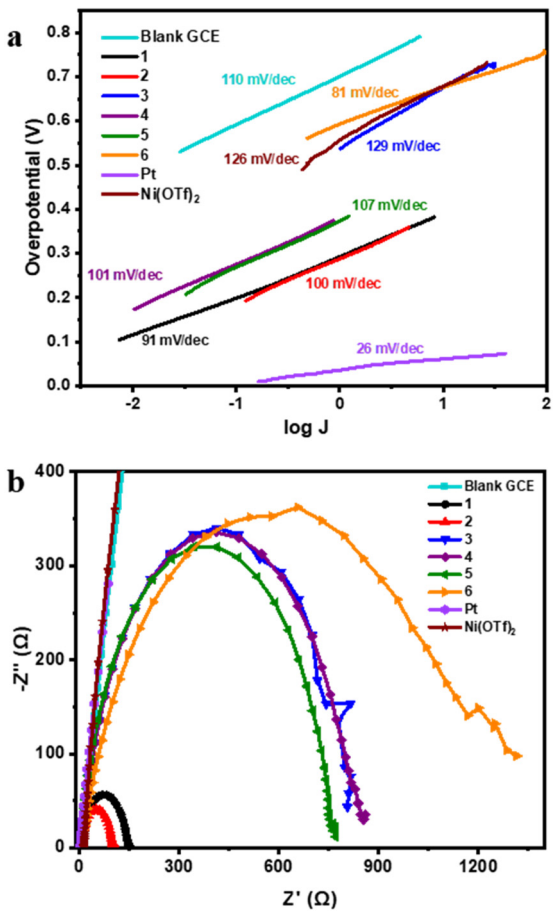

Fig. 3 (a) Tafel slope and (b) Nyquist plot of **1–6** in comparison to GCE, Pt, and $Ni(OTf)_2$ standards (after peak reductive cycling in 0.5 M aq. H_2SO_4).

Table 1 Overpotential, Tafel slope, and charge transfer resistance values for **1–6** after peak reductive cycling in comparison with standard electrodes GCE and Pt and with $Ni(OTf)_2$ using a GCE (in 0.5 M aq. H_2SO_4 electrolyte)

Electrode	Overpotential (V)	Tafel slope (mV dec^{-1})	Charge transfer resistance (Ω)
1	0.39	91	139
2	0.40	100	93
3	0.67	129	831
4	0.52	101	834
5	0.52	107	755
6	0.67	81	1143
GCE	>0.80	110	>50 000
Pt	0.06	26	1
GCE + $Ni(OTf)_2$	0.67	126	>20 000

plot of **1–6** at peak reductive cycle is shown in Fig. 3b and the values of charge transfer resistance are given in Table 1. Electrodes **1** and **2** display the lowest charge transfer resistance with values of 139 Ω and 93 Ω, respectively, which is reflective of their lowest overpotentials (near 0.40 V). For **4** and **5** the charge transfer resistance increases to 834 Ω and 755 Ω, respectively, in agreement with their greater overpotential (0.52 V) relative to **1** and **2**. Electrodes **3** and **6** have the highest charge transfer resistance values in their subgroups (**1–3**, **4–6**) with values of 831 Ω and 1143 Ω, respectively.

The surface morphology of the modified electrodes was investigated using SEM before and after 1000 reductive cycles. Prior to reductive cycling, needle-like crystalline outgrowths with the morphology of **Ni-2** [30] are observed on the surface of **2**, Fig. 4a and b. After 1000 CV cycles, a degradation in crystallinity is observed and the surface is more amorphous, Fig. 4c, although remnants of single crystals within the Nafion binder are visible upon magnification, Fig. 4d. The degradation of crystallinity following reductive cycling correlates with a significant reduction in overpotential and decreased charge transfer resistance. These improvements are attributed to the exposure of more active sites as the result of disruption of the surface by H_2 bubbling during reductive cycling. Extended reductive cycling ultimately leads to a gradual increase in overpotential due to depletion of catalyst material during periods of vigorous hydrogen evolution. The SEM images of **1** before and after reductive cycling (Fig. S22†) are similar to those of **2**, consistent with their similar changes in overpotential and charge transfer resistance upon reductive cycling. In contrast to **1** and **2**, **4** and **5** exhibit amorphous surfaces prior to reductive cycling due to the decreased tendency of **Ni-4** and **Ni-5** to crystallize, Fig. S24 and S25.† After 1000 reductive cycles, the surfaces are more fractured, which correlates with enhanced HER activity. Notably, the surfaces of **3** and **6** show well-defined microcrystals that are largely unperturbed by reductive cycling, Fig. S23 and S26.† This can be attributed to the lower basicity of **Ni-3** and **Ni-6** resulting in less HER activity during reductive cycling. Consequently, reductive cycling has a negligible impact on the performance of **3** and **6**.

Elemental mapping of the electrode surfaces by EDS before and after 1000 reductive cycles was performed to evaluate the effect on surface composition. Fig. 5a and b show the elemental mapping of nickel, nitrogen, and sulfur on the surface of **2** before and after 1000 reductive cycles, respectively. Each of the elements remain evenly distributed throughout the sample before and after reductive cycles. The EDS mapping plot depicted in Fig. 5c shows clearly defined nickel L_α and K_α peaks along with nitrogen and sulfur K_α peaks. Peaks for fluorine and oxygen from the Nafion binder can also be observed. A slight decrease in the intensity of the nickel peak after reductive cycling is observed, which is associated with the loss of catalyst from the electrode surface. EDS mapping of **1**, **4**, and **5** (Fig. S27, S29, and S30†) show a similar even distribution of nickel and other elements with a slight decrease in the peak intensity of nickel after 1000 reductive cycles. Interestingly, the EDS mapping plots of **3** and **6** (Fig. S28 and S31†), which do not show improvement in overpotential after reductive cycling, show no decrease in the peak intensity of nickel after reductive cycling. This is consistent with the observation in the SEM

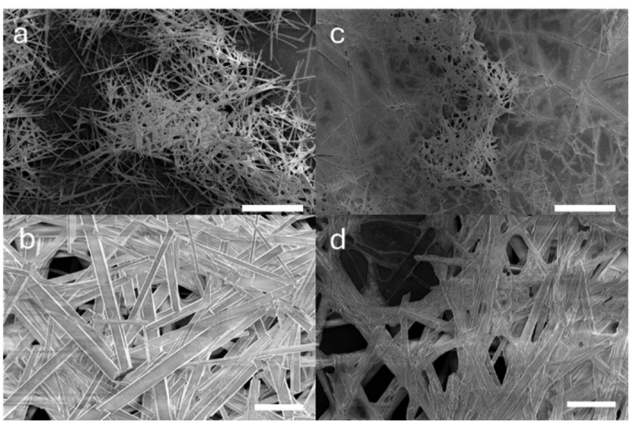

Fig. 4 SEM images of **2** (a, b) as drop cast on GCE and (c, d) after 1000 reductive cycles. Scale bars in a and c correspond to 100 μm and in b and d to 5 μm.

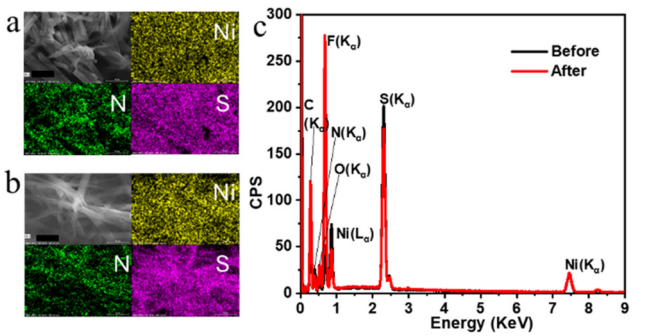

Fig. 5 Elemental mapping of **2** (a) as drop cast on GCE, showing SEM image (grayscale), nickel (yellow), nitrogen (green) and sulfur (pink) and (b) after 1000 reductive cycles. Scale bars at the bottom of SEM image correspond to 10 μm. (c) Comparative elemental plot before and after 1000 reductive cycle.

scan, where no changes in the surface morphology of the catalyst were observed even after 1000 reductive cycles.

In addition to the EDS mapping, XPS data were collected on **2** as a representative sample to verify the stability of the catalyst film after reductive cycling. The survey scans of **2** before and after 1000 reductive cycles are shown in Fig. S32.† Both scans display a prominent fluorine peak associated with the Nafion binder, along with nitrogen, sulfur, and nickel peaks from the catalyst. The similarities in the survey spectra before and after reductive cycling are consistent with retention of the catalyst structure. Fig. 6a shows the fitted peaks of the cationic nickel region. The high-resolution spectra of the core Ni 2p peak before cycling, Fig. 6a, shows a doublet at 854.6 eV and 871.82 eV (with satellite peaks) corresponding to $2p_{3/2}$ and $2p_{1/2}$, respectively, consistent with Ni^{2+} oxidation state. A comparison of high-resolution scans of the nickel region before and after reductive cycling, Fig. 6b, shows overlapping Ni $2p_{3/2}$ and Ni $2p_{1/2}$ peaks and satellites indicating no change in oxidation state.

To further confirm the stability of the catalyst, the XRD patterns of **1–3** were evaluated before and after reductive cycling. As shown in Fig. S34,† the pattern for **2** shows no change in peak positions after cycling, indicating the catalyst structure remains intact. A decrease in peak intensities was observed, which indicates a loss of the catalyst from the surface during reductive cycling. Similarly, comparative XRD diffraction patterns of **1** (Fig. S33†) show decreases in peak intensity after reductive cycling but no changes in peak positions. Interestingly, the XRD pattern of **3** (Fig. S35†) shows only minimal changes in peak intensities after reductive cycling with no change in peak position, supporting the SEM observation that the catalyst surface is not affected by reductive cycling.

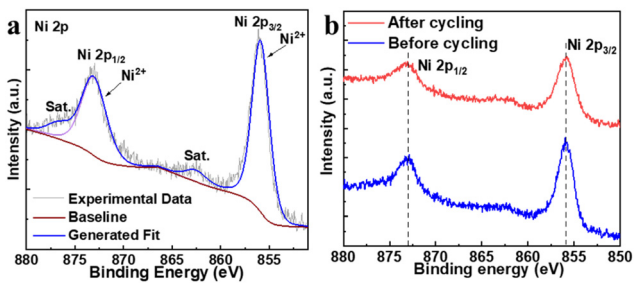

Fig. 6 XPS data for **2** showing (a) the fitted Ni^{2+} data before reductive cycling and (b) the Ni region before and after 1000 reductive cycles.

Table 2 Reduction potential, pK_a, and homogeneous overpotentials using acetic acid as a proton source and aqueous overpotentials for electrodes **1–6** (using 0.5 M H_2SO_4)

Complex	Reduction potential (V *vs.* Fc)	pK_a	Homogeneous overpotential (V *vs.* Fc)	Heterogeneous overpotential (V *vs.* RHE)
Ni-1	−1.73	7.38	0.76	0.39
Ni-2	−1.56	7.06	0.79	0.40
Ni-3	−1.38	<5	0.79	0.67
Ni-4	−1.60	7.61	0.80	0.52
Ni-5	−1.42	6.88	0.82	0.52
Ni-6	−1.24	<5	0.82	0.67

Conclusions

A series of modified electrodes **1–6** were prepared and their heterogeneous HER activity compared to our previously reported study on the homogeneous HER activities of **Ni-1–Ni-6**. Typically, homogeneous studies of molecular catalysts have the advantage of allowing systematic variation of the catalyst electronic structure to probe or modulate the reaction mechanism. In contrast, heterogenous HER is considered more practical for applications, but more difficult to study *via* systematic variation. Interestingly, our prior study of **Ni-1–Ni-6** demonstrated the ability to tune the electronic structure of the catalyst *via* ligand design, but with negligible effects on the HER overpotential under homogeneous conditions, Table 2. This was attributed degradation of the **Ni-1–Ni-6** catalysts to a common species under acidic and reducing conditions in acetonitrile. However, the complexes were stable after immobilization allowing evaluation of the structure–activity relationship under heterogeneous conditions in the current study.

The **Ni-1–Ni-6** catalysts were immobilized on GCEs to promote stability allowing for systematic variation of the HER overpotential under heterogeneous conditions. As highlighted in Table 2, electrodes prepared with **Ni-3** and **Ni-6** have the highest overpotential despite their accessible reduction potentials as the catalyst lack significantly basic sites for protonation. The HER activity of modified GCEs **1**, **2**, **4**, and **5** was optimized by reductive cycling, which increased the number of active sites and reduced charge transfer resistance. Electrodes **1** and **2** had the lowest heterogenous HER overpotentials as they contain accessible thiosemicarbazonato groups. The introduction of bulky phenyl groups in the catalysts structure of **4** and **5** restrict H^+ accessibility to the hydrazino nitrogen of the thiosemicarbazonato group increasing overpotential relative to **1** and **2**. In contrast to most systems where the homogeneous HER method is good for systematic evaluation of ligand effects on the mechanism or HER activity and heterogeneous HER method is good for practical application of catalyst, this study is a rare example of a molecular catalysts system where immobilization is required for both systematic HER activity study and practical application.

Author contributions

S. K. performed some ligand and metal complex syntheses and measurements of faradaic efficiency, N. A. conducted XRD experiments, S. C. performed XPS studies, and J. H. assisted with SEM and EDX studies. M. P. performed all other experiments and wrote the first draft of the manuscript. D. T. H., G. G., R. M. B., and C. A. G. conceived the project, supervised

experimental studies, and contributed to writing the manuscript. All authors have approved the final version of the manuscript.

Data availability

The data supporting this article have been included as part of the ESI.†

Conflicts of interest

There are no conflicts to declare.

Acknowledgements

This research was supported by the National Science Foundation CHE-1955268 (CAG) and CHE-1800245(RMB). The Department of Energy (DEFG02-08CH11538) and the Kentucky Research Challenge Trust Fund are acknowledged for upgrade of the X-ray facility (MSM).

References

1 J. M. Ogden, *Phys. Today*, 2002, **55**, 69–75.
2 H. B. Gray, *Nat. Chem.*, 2009, **1**, 7–7.
3 S. Dorel, M. Lucian, L. Gheorghe and L. G. Cristian, *Processes*, 2024, **12**, 1651.
4 J. N. Hansen, H. Prats, K. K. Toudahl, N. Mørch Secher, K. Chan, J. Kibsgaard and I. Chorkendorff, *ACS Energy Lett.*, 2021, **6**, 1175–1180.
5 C. Sealy, *Mater. Today*, 2008, **11**, 65–68.
6 Y. Yang, Y.-T. Shao, X. Lu, Y. Yang, H.-Y. Ko, R. A. DiStasio Jr., F. J. DiSalvo, D. A. Muller and H. D. Abruña, *J. Am. Chem. Soc.*, 2022, **144**, 15698–15708.
7 J. Wang, X. Yue, Y. Yang, S. Sirisomboonchai, P. Wang, X. Ma, A. Abudula and G. Guan, *J. Alloys Compd.*, 2020, **819**, 153346.
8 M. Zeng and Y. Li, *J. Mater. Chem. A*, 2015, **3**, 14942–14962.
9 Y. Jiao, Y. Zheng, M. Jaroniec and S. Z. Qiao, *Chem. Soc. Rev.*, 2015, **44**, 2060–2086.
10 L. Dai, *Curr. Opin. Electrochem.*, 2017, **4**, 18–25.
11 H. H. Do, T. H. C. Nguyen, T. V. Nguyen, C. Xia, D. L. T. Nguyen, P. Raizada, P. Singh, V.-H. Nguyen, S. H. Ahn, S. Y. Kim and Q. V. Le, *Int. J. Hydrogen Energy*, 2022, **47**, 37552–37568.
12 Y. Zhu, Q. Lin, Y. Zhong, H. A. Tahini, Z. Shao and H. Wang, *Energy Environ. Sci.*, 2020, **13**, 3361–3392.
13 D. Liu, G. Xu, H. Yang, H. Wang and B. Y. Xia, *Adv. Funct. Mater.*, 2023, **33**, 2208358.
14 Z.-G. Yang, H.-M. Xu, T.-Y. Shuai, Q.-N. Zhan, Z.-J. Zhang, K. Huang, C. Dai and G.-R. Li, *Nanoscale*, 2023, **15**, 11777–11800.
15 Y. Gong, J. Yao, P. Wang, Z. Li, H. Zhou and C. Xu, *Chin. J. Chem. Eng.*, 2022, **43**, 282–296.
16 F. Zaccaria, G. Menendez Rodriguez, L. Rocchigiani and A. Macchioni, *Front. Catal.*, 2022, **2**, 892183.
17 R. Jain, M. S. Mashuta, R. M. Buchanan and C. A. Grapperhaus, *Eur. J. Inorg. Chem.*, 2017, **2017**, 3714–3719.
18 T. Straistari, R. Hardré, J. Fize, S. Shova, M. Giorgi, M. Réglier, V. Artero and M. Orio, *Chem. – Eur. J.*, 2018, **24**, 8779–8786.
19 R. Jain, A. A. Mamun, R. M. Buchanan, P. M. Kozlowski and C. A. Grapperhaus, *Inorg. Chem.*, 2018, **57**, 13486–13493.
20 A. Z. Haddad, S. P. Cronin, M. S. Mashuta, R. M. Buchanan and C. A. Grapperhaus, *Inorg. Chem.*, 2017, **56**, 11254–11265.
21 T. Straistari, R. Hardré, J. Massin, M. Attolini, B. Faure, M. Giorgi, M. Réglier and M. Orio, *Eur. J. Inorg. Chem.*, 2018, **2018**, 2259–2266.
22 A. Z. Haddad, B. D. Garabato, P. M. Kozlowski, R. M. Buchanan and C. A. Grapperhaus, *J. Am. Chem. Soc.*, 2016, **138**, 7844–7847.
23 W. Zhang, A. Z. Haddad, B. D. Garabato, P. M. Kozlowski, R. M. Buchanan and C. A. Grapperhaus, *Inorg. Chem.*, 2017, **56**, 2177–2187.
24 N. Kaeffer, A. Morozan, J. Fize, E. Martinez, L. Guetaz and V. Artero, *ACS Catal.*, 2016, **6**, 3727–3737.
25 V. Artero and M. Fontecave, *Chem. Soc. Rev.*, 2013, **42**, 2338–2356.
26 L. Chen, G. Chen, C.-F. Leung, S.-M. Yiu, C.-C. Ko, E. Anxolabéhère-Mallart, M. Robert and T.-C. Lau, *ACS Catal.*, 2015, **5**, 356–364.
27 A. J. Gupta, N. S. Vishnosky, O. Hietsoi, Y. Losovyj, J. Strain, J. Spurgeon, M. S. Mashuta, R. Jain, R. M. Buchanan, G. Gupta and C. A. Grapperhaus, *Inorg. Chem.*, 2019, **58**, 12025–12039.
28 A. Gupta, K. Ankireddy, B. Kumar, A. Alruqi, J. Jasinski, G. Gupta and T. Druffel, *Nanotechnology*, 2019, **30**, 175401.
29 M. Paudel, B. Daniels, A. M. Arts, A. Gupta, T. Kalbfleisch, D. T. Hofsommer, C. A. Grapperhaus, R. M. Buchanan and G. Gupta, *New J. Chem.*, 2022, **46**, 18832–18838.
30 M. Paudel, S. Karki, K. Bajaj, D. T. Hofsommer, S. Parmar, M. S. Mashuta, P. M. Kozlowski, G. Gupta, R. M. Buchanan and C. A. Grapperhaus, *Inorg. Chim. Acta*, 2024, **572**, 122254.
31 D. X. West, J. S. Ives, G. A. Bain, A. E. Liberta, J. Valdés-Martínez, K. H. Ebert and S. Hernández-Ortega, *Polyhedron*, 1997, **16**, 1895–1905.
32 S. A. Andres, K. Bajaj, N. S. Vishnosky, M. A. Peterson, M. S. Mashuta, R. M. Buchanan, P. J. Bates and C. A. Grapperhaus, *Inorg. Chem.*, 2020, **59**, 4924–4935.
33 H. Beraldo, S. B. Kaisner, J. D. Turner, I. S. Billeh, J. S. Ives and D. West, *Transition Met. Chem.*, 1997, **22**, 459–464.
34 T. Shinagawa, A. T. Garcia-Esparza and K. Takanabe, *Sci. Rep.*, 2015, **5**, 13801.

